IEEE Access
Multidisciplinary | Rapid Review | Open Access Journal

Received April 28, 2020, accepted May 8, 2020, date of current version June 10, 2020.

Digital Object Identifier 10.1109/ACCESS.2020.2994072

Modeling of the Distribution of Undeformed Chip Thickness Based on the Real Interference Depth of the Active Abrasive Grain

MINGXIA KANG, LU ZHANG, AND WENCHENG TANG
School of Mechanical Engineering, Southeast University, Nanjing 210000, China

Corresponding author: Wencheng Tang (k18351987@163.com)

This work was supported in part by the National Natural Science Foundation of China under Grant 51675100, and in part by the National CNC Equipment Major Project under Grant 2016ZX04004008.

ABSTRACT Distribution of the maximum undeformed chip thickness can be approximated as the reproduction of grooves and protrusions of the grinding surface. It plays a very important role in grinding process as it has a close influence on the prediction and modeling of grinding forces, tool life, and surface quality, as well as process stability. In this study, it is investigated from the perspective of the real interference depth of the active abrasive grain to cater to the performance evaluation of the grinding surface. Firstly, image processing techniques combined with three dimensional topography tests are utilized to extract grains' essential characteristics such as the protrusion height, shape, distribution and density. Then, grains' wear is quantified by the probability assignment function and Dempster-Shafer evidence theory. Based on this, the actual interference depth of a single grain is determined. Through grain's kinematics analysis and considering the effect of contact deformation on the actual contact arc length and affective cutting edge density, the distribution of chip thickness in the current grinding area is defined and its distribution model is established. Model's correctness and rationality are verified by grinding experiments of the slider raceway. Results demonstrate the grain's interference depth highly depends on its protrusion height, wear amount and grinding depth which is a primary contributor to the size of undeformed chip thickness, and grains' density, contact deformations mainly affect its distribution. The quantified distribution model of the maximum undeformed chip thickness lays a foundation for the topography modeling and integrity research of grinding surfaces.

INDEX TERMS Abrasive particles wear, active cutting edges, grinding, image processing, interference depth, protrusion height, undeformed chip thickness.

I. INTRODUCTION

Grinding is the material removal process on which abrasives are fixed to a grinding tool or a grinding wheel [1]. With its incomparable advantages to other machining methods (e.g., turning, milling, drilling), it is the most widely used operation available for the hard and brittle materials or other materials, such as quenched steel, high-strength alloy steel and cemented carbide. However, the morphology and the cutting edge geometry of abrasive particles during the grinding process are constantly changing due to the wear and fracture of abrasive grains. Accordingly, it is also more complicated than conventional machining operations [2]. Similar to other machining methods such as turning or milling, material removal of grinding occurs mainly by the formation of chips,, but the chip is on a much finer scale which is realized by the interactions between a large number of cutting grains and a workpiece [3]. Abrasive particles are stochastically distributed on the wheel surface and the orientations and positions relative to the workpiece are irregular which result in a large variation in the interference depth between the grains and the workpiece. Consequently, the interaction is seriously hard to be experimentally examined as a result of the superposition of the material removal of abrasive grains with different sizes and shapes [4]–[6]. However, the undeformed chip thickness or the maximum undeformed chip thickness (MUCT) can be utilized to characterize the single grit-workpiece interaction and a large amount of attention

The associate editor coordinating the review of this manuscript and approving it for publication was Zhixiong Peter Li.

and attempts have been put on the establishment of the undeformed chip thickness or MUCT theoretical model.

An earlier method to determine MUCT is based on an assumption that cutting points are equally spaced around the wheel periphery. The MUCT is obtained by assuming the cutting path as a circular arc [7].

$$h_m = 2L\frac{v_w}{v_s}\sqrt{\frac{a}{d_e}} \tag{1}$$

where h_m is the MUCT, v_w is the workpiece feeding speed, v_s is the wheel speed, a is the depth of cut, d_e is the equivalent diameter of a wheel and L is the space between active grains which is difficult to be determined. Malkin [7] pointed out that the number of cutting points is equal to the product of the circumferential area of the grinding wheel and the number of cutting points per unit area C. For simplicity, the MUCT is modeled as having a rectangular cross-section and it is expressed as:

$$h_m = \left[\frac{4}{Cr}\left(\frac{v_w}{v_s}\right)\left(\frac{a}{d_e}\right)^{1/2}\right]^{1/2} \tag{2}$$

where r is the chip width-to-thickness ratio. Another method to calculate the MUCT is based upon a material balance between the volume of chips produced at the cutting points and the overall removal rate. Considering a chip with a triangular cross-section, the MUCT is [7]:

$$h_m = \left[\frac{6}{Cr}\left(\frac{v_w}{v_s}\right)\left(\frac{a}{d_e}\right)^{1/2}\right]^{1/2} \tag{3}$$

In both cases, the MUCT is equal to an average value of the undeformed chip thickness since abrasive grains are presumed uniformly distributed. Actually, the grains' protrusion heights are stochastic and the interference depth between particles and the workpiece is considerably different. The distribution of chip thickness is governed mainly by the interference depth and stochastic distribution of cutting edges on the wheel surface. Abrasive grain with a larger protrusion height brings in a sizeable chip thickness. Conversely, no chip is produced due to the sliding or plowing of grains with a small protruding height. To account for this, the Rayleigh probability function [8], [9] is presented to describe the stochastic interference depth of grains which is equal to the undeformed chip thickness,

$$f(h) = \begin{cases} (h/\sigma^2)e^{-h^2/2\sigma^2} & h \geq 0 \\ 0 & h < 0 \end{cases} \tag{4}$$

with an expected value and the variance expressed as

$$E(h) = \sqrt{\pi/2}\sigma \tag{5}$$

$$sd(h) = \sqrt{0.429}\sigma \tag{6}$$

where h is the undeformed chip thickness and σ is the parameter defining this function. The Rayleigh distribution touches upon strong assumptions and σ has no clear physical meaning [10]. To further conform to the real situation of abrasive grains distribution, the Monte Carlo method [11] and the vibration method [12] are utilized to randomly generate the diameter and distributed position of the grain. However, they are both accompanied by large random errors, uncertainty and longer modeling time. To overcome the above problems, the distribution, size and shape of abrasive particles are identified from the measured wheel topography with image processing techniques in this paper.

In addition, the real contact arc length and the number of active cutting edges are influenced by the contact deformation in the grinding zone which inevitably brings in a change in the MUCT distribution. Rowe *et al.* [13] propose the real contact arc length:

$$l_c = (ad_e + 8Rr^2F_n'd_e(K_s + K_w))^{1/2} \tag{7}$$

It consists of the ideal contact arc length $(ad_e)^{1/2}$ and the change of contact arc length due to wheel-workpiece contact deformation resulted from the normal force F_n' per length.

$$K_i = \frac{1-\upsilon_i^2}{\pi E_i} i = s(wheel),\ w(workpiece), g(grit) \tag{8}$$

where E_i and υ_i are the modulus of elasticity and Poisson's ratio for the wheel and the workpiece material, respectively. Apart from the wheel body deformation, the grain also has a microscopic contact deformation [9] and their Hertz relations are as follows, respectively.

$$\delta = \sqrt[3]{(3\pi/2\sqrt{2})^2(K_w + K_g)^2(1/d_g)F_{ng}^2} \tag{9}$$

$$l_c' \cong 2\sqrt{d_s\delta} \tag{10}$$

$$a' = \sqrt{2.56(\pi d_s/b)(K_w + K_s)F_n} \tag{11}$$

$$l_c'' \cong l_c' + a' \tag{12}$$

where δ, a' and F_{ng}, F_n and d_g, d_s are the elastic deflections, normal loads and diameters of the grit and wheel, respectively. l_c' is the contact length only considering the microscopic contact deformation of grits. l_c'' is the total contact arc length.

However, little studies simultaneously consider grains' random distribution and contact deformations. Additionally, particles' wear also has a significant effect on undeformed chip thickness as different wear states could produce dissimilar material removal behaviors during grinding [14]–[16]. Numerous researches have investigated the grit wear behavior based on a single grain [17]–[20]. It is mainly carried out from process parameters, bond volume, grain size, grain embedding depth, grinding load and other aspects [5], [21]–[23]. Results demonstrate that the rake angle, grain shape, and grinding load has great influence on the wear resistance of abrasive grains. However, only the qualitative analysis of the abrasive wear are conducted by the majority of researches [15], [16], [23]–[26], and it has not been converted into the impact on the undeformed chip thickness.

In this paper, MUCT distribution is studied from the perspective of the actual interference depth of abrasive particles by considering three classifications influencing factors.

TABLE 1. The dressing experiments and the obtained AAG number in six different areas of each wheel and density (/mm^2).

Number	Dressing feed rate (mm / min)	Dressing depth (mm)	Drssing speed (m / s)	90-100 μm	100-110 μm	110-160 μm	3D test AAG	SEM test AAG	3D test density	SEM test density
S1	0.374	0.4	18	12	3	36	51	55	21	23
S2	0.436	0.5	21	4	10	34	48	53	21	22
S3	0.698	0.4	21	8	7	24	39	45	17	19
S4	0.698	0.5	24	6	7	37	50	55	21	23
S5	0.710	0.6	18	5	5	43	53	60	22	25
S6	1.076	0.4	24	5	5	33	43	52	19	22
S7	1.099	0.6	21	5	8	25	38	47	17	20
S8	0	0	0	6	5	36	47	58	20	25

The first type is characterization parameters for quantifying the shape, protrusion height, number and distribution of abrasive particles. The second type is the quantification of abrasives' wear or fracture during the grinding process. The third type is the contact deformations in wheel-workpiece and grain-workpiece zones.

II. THE ESSENTIAL CHARACTERISTICS OF THE ACTIVE ABRASIVE GRAIN

Chip is produced by interactions of the interference portion between an active abrasive grain (AAG) with the workpiece. AAG is the grain contacting the workpiece surface and participating in the removal of the surface material. To characterize the undeformed chip thickness more accurately, the size, shape, protrusion height, distribution, and density of the AAG are firstly extracted from the wheel topography.

A. THE SHAPE AND SIZE OF THE AAG

From a scanning electron microscope (SEM) of the abrasive grain morphology obtained in our previous work, the AAG shape after dressing is simplified into an arbitrary pyramid which is expressed in [27]. According to the AAG volume ratio t_1 and apex angle α identified by image processing techniques, the protruding height h and width a of an AAG are

$$h = R\sqrt[3]{\pi t_1/(\tan^2\frac{\alpha}{2})} \tag{13}$$

$$a \approx 2h\tan(\alpha/2) \tag{14}$$

where R is the grain radius before the wheel dressing. The wheel type is *1A46 × 25 × 13-SA100K-35* with a particle size of 100#. Thus, R is ranging from 62.5 μm to 80 μm. To ensure the accuracy of results, α is extracted from six different areas of each grinding wheel, as described in [27]. It follows a normal distribution whose mean value and standard deviation are 81.2841, 21.6540, respectively.

$$f(\alpha) = \frac{1}{\sqrt{2\pi}\times 21.654}\exp(-\frac{(\alpha-81.2841)^2}{2\times 21.654^2}) \tag{15}$$

Accordingly, the apex angle, width, protrusion height of an AAG is determined.

B. THE DENSITY AND DISTRIBUTION OF AAG

In practice, not all abrasive grains are AAG and the protruding height is the main criterion for determining whether the abrasive particles can participate in grinding. During the grinding process, the heights of abrasive particles are gradually reduced to a more uniform value because of the AAG wear. According to the wheel experiments before and after grinding carried out by Kang *et al.* [27], the abrasive grain after dressing with a height of more than 87 μm is AAG. AAG number and density are shown in Table 1 after analyzing six different locations areas of each wheel with the same size 793 μm × 586 μm. Since the count is the abrasive grains larger than 90 μm in 3D measurement, the AAG density is slightly smaller than that measured by the SEM. They are 17-22/mm^2 and 19-25/mm^2, respectively. Herein, 21/mm^2 is utilized as the AAG density when establishing the MUCT distribution model.

Comparing the wheel SEM images obtained from the dressing experiments, 1/3 of the black area ratio is assumed as the largest abrasive overlap rate. To avoid the concentrated phenomenon that abrasive particles are overlapped or separated, a method of randomly distributed in the circumferential direction of the grinding wheel and evenly distributed in its axial direction is proposed. The acquired distance between two adjacent abrasive grains in the circumferential direction and the axial direction are expressed in (63, 65, 67, 69), respectively by Kang *et al.* [27]. Since chips are generated by grinding motions of the interference parts between AAGs and workpiece, the shape, size, distribution or density of chips can be further investigated after determining that of the abrasive grain.

III. THE SHAPE, SIZE AND DISTRIBUTION OF CHIPS

From Fig. 1 (a), movements mainly consist of rotating and radial feeding of the wheel and the feeding of the working platform in the grinding process of slider raceway surfaces. The wheel needs trimming to the cross-sectional shape of the slider and its two symmetrical circular table surfaces are the primary grinding areas, as expressed in Fig.1 (b). The AAG is large in number and randomly distributed on the wheel surface (Fig.1 (c-d)). Details of the chip generation and material removal are determined by AAG natures, workpiece properties, the grinding force magnitude, and the grinding

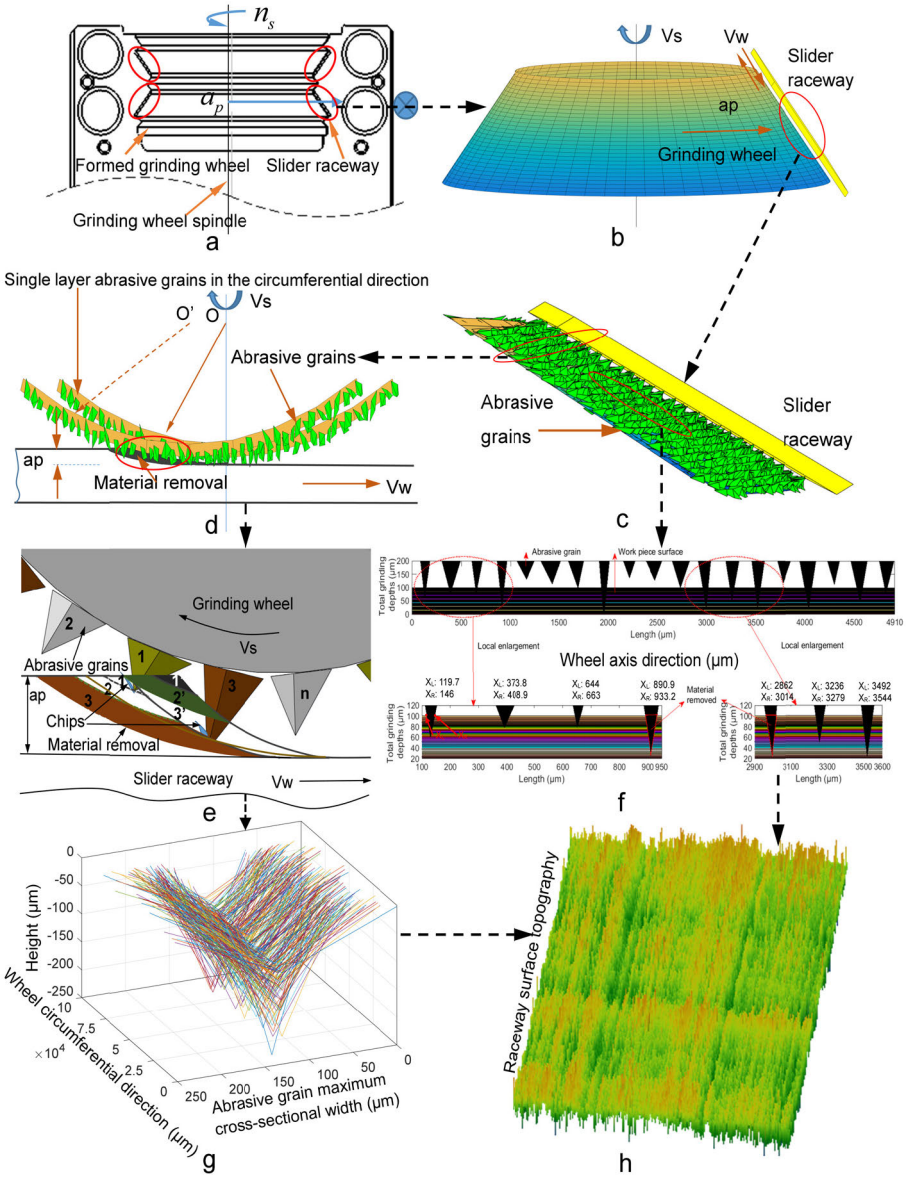

FIGURE 1. **(a) Schematic diagram of the grinding movements. (b) Partial enlarged image of the wheel. (c) Abrasive grains on the wheel surface. (d) Grinding between the AAG and workpiece. (e) Chip formation process. (f) Distribution of the interference depths. (g) Cross-sectional profiles. (h) Surface topography of the raceway surface.**

fluid, etc. Xu *et al.* [2] highlighted that the physics and chemistry involved are complex and only understood on the basis of greatly simplified models. In this paper, the undeformed chip thickness is investigated based on the interference depth of the AAG tip penetration into the workpiece. And the interference depth of AAG sliding or plowing on the workpiece surface is regarded as undeformed chip thickness which is also argued by Zhang *et al.* [10]. It is manifested clearly in Fig.1 (e-f) that the interference depth is strongly influenced by AAG protruding height and the grinding depth. Contrast to grain 1, grain 3 with a higher protruding height has a greater interference depth accompanied by a larger chip. Fig.1(g) exhibits the cross-sectional profiles of all the abrasive grains in a certain circumferential direction of the wheel. Their accumulated cutting effects are grooves and bulges in the grinding direction on the surface topography, as shown in Fig.1 (h). Based on the above analysis, the influence of the size, protrusion height of a single AAG on the chip generation is discussed firstly.

A. THE CHIP THICKNESS GENERATED BY A SINGLE AAG

The cutting trajectories of two AAGs with different protruding heights are indicated in Fig.2. *AAGm* in up-grinding contacts the workpiece at point M and follows the curved path to point B_m at which *AAGm* separates with the workpiece surface. The generated chip is displayed by the cross-hatched

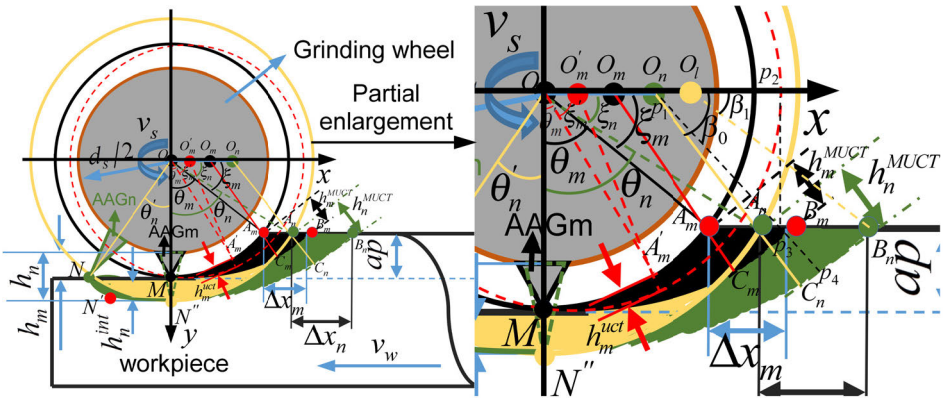

FIGURE 2. The chip generation process of two AAGs with different protrusion heights.

area $MA_mB_mC_mM$ in Fig.2. The cutting path MC_mB_m is a cycloid produced by the superposition of the wheel circular motion and the workpiece tangential motion which can be approximated by a circular arc [3].

With the feeding motion of the workpiece, the previous cutting point is followed the same geometrical path shape but displaced by the distance A_mB_m which is the feed amount s per cutting point. It is equal to the product of the feed velocity and the time L/v_s between successive cuts:

$$s = \frac{Lv_w}{v_s} \tag{16}$$

where L is the space between successive cutting points. Different from the definition mentioned by Malkin and Guo [3], herein, L is determined by the rotation angle of the dynamic cutting point and the AAG protruding height.

$$L = \theta r \tag{17}$$

$$r = d_s/2 + h \tag{18}$$

where θ is the rotated angle that AAG and workpiece from contact to separation. r is the distance of the wheel center to the contact point between the AAG and the workpiece. The geometric relationship of the chip formation trajectory is apparently revealed from the enlarged partial view of Fig. 2. The chip thickness generated by $AAGm$ h_m^{uct} is calculated as:

$$h_m^{uct} = r_{AAGm} - O'_mA'_m \tag{19}$$

From $\triangle OO'_mA'_m$,

$$O'_mA'_m = \sqrt{\left(OO'_m\right)^2 + r_{AAGm}^2 - 2r_{AAGm}OO'_m cos\xi'_m} \tag{20}$$

$$\xi'_m = \frac{\pi}{2} - \theta'_m \tag{21}$$

$$OO'_m = \theta'_m r_{AAGm} \tag{22}$$

Compared with MC_mB_m, the chip formation trajectory of $AAGn$ is $NN'N''C_nB_n$ which is denoted in Fig.2. $AAGn$ contacts the workpiece at point N and follows the curved path to point B_n and the area $NN'N''C_nB_nA_mMN$ enclosed is the generated chip. Due to the larger protruding height of $AAGn$, it has a greater interference depth, and the undeformed chip thickness generated is larger than that of $AAGm$. It shows that the undeformed chip thickness increases with the rising protrusion height. In addition, the undeformed chip thickness is constantly changing during the generation of the whole chip. Taking $AAGn$ as an example, the generated process of a complete chip can be divided into three stages according to the geometric relationship in Fig.2. They are the generation of cutting trajectories NN'', $N''C_n$ and C_nB_n, respectively. Taking the interference depth into account, the chip thickness at any time t_i in the first and second stages is as follows, respectively according to (16) - (22).

$$h_{ti}^{uct} = \left(r - \left(r^2A^2\theta_i^2 + r^2 - 2r^2A\theta_i\left(\theta'_n + \theta_i\right)\right)^{1/2}\right) \Big/ \times N\left(\theta_i \in \left[-\theta'_n, 0\right)\right) \tag{23}$$

$$h_{ti}^{uct} = r - \left(r^2A^2\theta_i^2 + r^2 - 2r^2A\theta_i^2\right)^{1/2} + h_{int}\left(\theta_i \in [0, \theta_n]\right) \tag{24}$$

$$cos\theta'_n = \frac{d_s/2 + h_0}{r} \tag{25}$$

$$cos\theta_n = \frac{r - ap - h_{int}}{r} \tag{26}$$

$$h_{int} = \frac{h - h_0}{N} \tag{27}$$

$$N = \frac{grinding\ amount}{ap} \tag{28}$$

$$A = \frac{v_w}{v_s} \tag{29}$$

where d_s is the wheel diameter and it is in 35-45 mm. h_{int} is the interference depth of an AAG in the single feeding process. N is the feeding number when the grinding amount is up to 0.1 mm in this paper. The third stage is the formation of C_nB_n. It starts with MUCT and ends with the separation of the AAG from the workpiece. The chip thickness h_{ti}^{uct} at any time t_i in the third stage is equal to the length p_3p_4 which is

$$p_3p_4 = p_1p_4 - p_1p_3 \tag{30}$$

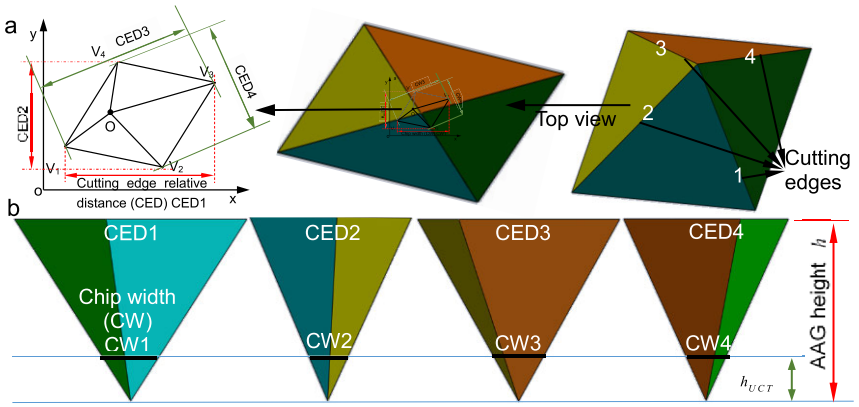

FIGURE 3. The largest sectional-surface of the chip.

where p_1p_4 is the same as r. From $\triangle p_1p_2p_3$,

$$p_1p_3 = p_2p_3 / sin\beta \ (\beta \in [\beta_0, \beta_1]) \tag{31}$$

$$p_2p_3 = d_s/2 + h_0 - ap \tag{32}$$

$$h_{ti}^{uct} = r - \frac{d_s/2 + h_0 - ap}{sin\beta} \quad (\beta \in [\beta_0, \beta_1]) \tag{33}$$

where β is gradually reduced to the minimum value β_1 from the maximum value β_0. β_0 and β_1 are written as (34) and (35), respectively. The relationship between β and θ_i is denoted as (36).

$$\beta_0 = arcsin\left(\frac{d_s/2 + h_0 - ap}{r - h^{muct}}\right) \tag{34}$$

$$\beta_1 = arcsin\left(\frac{d_s/2 + h_0 - ap}{r}\right) \tag{35}$$

$$\beta = arccos\frac{\left(r - h_{ti}^{uct}\right)^2 + r^2 - \theta_i^2 r^2 A^2}{2r\left(r - h_{ti}^{uct}\right)} + \frac{\pi}{2} - \theta_i \tag{36}$$

Comparing the undeformed chip thickness generated in three stages, the MUCT is generated when θ_i is up to θ_n.

$$h^{muct} = r - \left(r^2A^2\theta_n^2 + r^2 - 2r^2A\theta_n^2\right)^{1/2} + h_{int} \tag{37}$$

The sum of the entire chip thickness produced by a single AAG is calculated as

$$h_{sum}^{uct} = \int_{-\theta_n'}^{0} \left[r - \left(r^2A^2\theta^2 + r^2 - 2r^2A\theta\left(\theta_n' + \theta\right)\right)^{1/2} / N\right] d\theta + \int_{0}^{\theta_n} \left[r - \left(r^2A^2\theta^2 + r^2 - 2r^2A\theta^2\right)^{1/2} + h_{int}\right] d\theta + \int_{\beta_0}^{\beta} \left(r - \frac{d_s/2 + h_0 - ap}{sin\beta}\right) d\beta \tag{38}$$

As the influence of the feeding motion on undeformed chip thickness in $[-\theta_n', 0)$ is small, its calculation is simplified by an arc and the simplified sum and average of undeformed chip thickness is (39) and (40), respectively.

$$h_{sum}^{uct} = \int_{-rsin\theta_n'}^{0} \left(\sqrt{r^2 - x^2} - rcos\theta_n'\right) / N dx + \int_{0}^{\theta_n} \left[r - \left(r^2A^2\theta^2 + r^2 - 2r^2A\theta^2\right)^{1/2} + h_{int}\right] d\theta + \int_{\beta_0}^{\beta_1} \left(r - \frac{d_s/2 + h_0 - ap}{sin\beta}\right) d\beta \tag{39}$$

$$\overline{h_{sum}^{uct}} = r\left(\frac{4 - \sqrt{1 - \theta_n^2/B} - cos\theta_n'}{6} / N - \frac{\sqrt{B}arcsin\left(\theta_n/\sqrt{B}\right)}{6\theta_n} + \frac{arccos\left(sin\theta_n'\right) - \pi/2}{6sin\theta_n'N}\right) + \frac{h_{int}}{3} - \frac{6695ln\, sin\beta_0/sin\beta_1}{\beta_1 - \beta_0} \tag{40}$$

$$B = 1/\left(2A - A^2\right) \tag{41}$$

According to (17-18, 25-27, 37-40), it is clearly illustrated that the interference depth and protrusion height of the AAG are the primary factors to decide the MUCT size.

B. THE CHIP WIDTH GENERATED BY A SINGLE AAG

As the AAG is simplified into a random pyramid, the largest sectional-surface of the chip is a triangle, as expressed in Fig.3. And its size and shape are not simply dependent on the apex angle and the relative positions of four cutting edges of the AAG, but also on the undeformed chip thickness. According to the relative positions of the four cutting edges, the bottom sides of the triangle sectional-surface and the corresponding chip widths are *CED1, CED2, CED3, CED4*

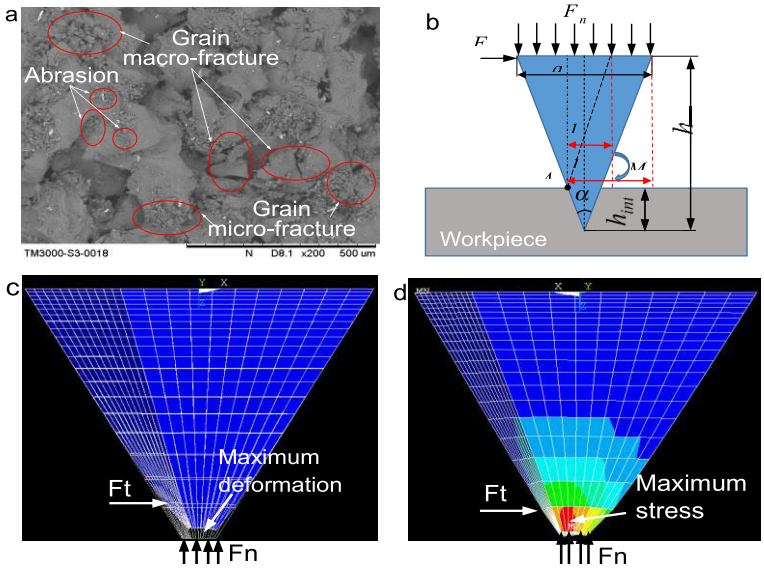

FIGURE 4. (a) Distribution of grains wear morphology; (b) The grinding forces and force torque acting on the AAG; (c) The FE analysis of the AAG deformation; (d) The FE stress analysis of the AAG.

and *CW1, CW2, CW3, CW4,* respectively. From the geometry relationship of the triangle in Fig.3 (b),

$$\frac{CW1}{CED1}=\frac{CW2}{CED2}=\frac{CW3}{CED3}=\frac{CW4}{CED4}=\frac{h_{UCT}}{h} \tag{42}$$

where, h_{UCT} refers to the maximum thickness of the chip produced by a single abrasive grain, which is equivalent to h^{MUCT}.

From the spatial coordinates of five apexes of a random and arbitrary pyramid presented by Kang *et al.* [27], *CED1, CED2, CED3, CED4* can be calculated as below.

$$CED1=X_{V3}-X_{V1}=a\,(c_1+c_2) \tag{43}$$

$$CED2=Y_{V4}-Y_{V2}=a\,(2-c_3-c_4) \tag{44}$$

$$CED3=|V_1V_3|=a\sqrt{(c_1+c_2)^2+(c_3+c_4)^2} \tag{45}$$

$$CED4=|V_2V_4|=a\sqrt{(2-c_1-c_2)^2+(2-c_3-c_4)^2} \tag{46}$$

To avoid generating seriously irregular abrasives, the range of random variables c_1, c_2, c_3, c_4 is assumed as 0.3-0.7. In consequently, the range of *CED1, CED2, CED3, CED4* is $[0.6a, \sqrt{3.92}a]$ and *CW1, CW2, CW3, CW4* is in $[0.6ah_{UCT}/h, \sqrt{3.92}ah_{UCT}/h]$ according to (42-46). However, it is considerably difficult to access the relative positions of four cutting edges when the AAG interferes with the workpiece. Herein, the chip width is determined by a method of randomly taking values in the range of $[0.6ah_{UCT}/h, \sqrt{3.92}ah_{UCT}/h]$.

In summary, the chip width, MUCT, average value of undeformed chip thickness and its value at any time generated by a single AAG can be determined after obtaining the h, a and α of the AAG by image processing techniques and 3D topography measurement. However, the AAG is continuously wearing during the grinding process as a result of the alumina brittleness. The protruding height of an AAG is decreased due to its abrasion or fracture which inevitably brings in a variation in the true interference depth between the AAG and workpiece and followed by the changing of undeformed chip thickness size. Accordingly, the influence of the AAG wear on undeformed chip thickness could not be ignored.

C. THE CHIP THICKNESS AND WIDTH OF A SINGLE AAG CONSIDERING ABRASIVE WEAR

Fig.4 (a) is the SEM image of the wheel surface topography in the grinding process. It can be noticed that the wear behavior of abrasive grains mainly includes abrasion on the flank face, grain micro-fracture, and grain macro-fracture three types. Although new micro-tips are generated during the grinding process, which may improve the self-sharpening ability of the AAG, they are too small relative to the AAG and easily worn away. Consequently, the AAG is gradually turned blunt. Moreover, undeformed chip thickness will be decreased due to the reduced interference depth caused by AAG wear. Esteban Fernández *et al.* [26] suggested that abrasive size and reinforcement exert a greater effect on abrasive wear than the load that is applied. Similar results are also reported by Spuzic *et al.* [28]. Herein, the material, force, temperature, and grinding parameters of abrasives are assumed to be constant and the joining between the AAG and binder is assumed strong enough without grain pullout. The influence of AAG's size on its wear is mainly quantitatively studied through mechanical analysis and finite element method.

In Fig.4 (a), most exfoliated bodies produced by abrasive abrasion are not powdery as a result of the brittle nature of

alumina abrasive grains. Its size does not exceed 10 μm which is similar to that induced by the micro-fracture while the size generate by the macro-fracture is larger than 20 μm. Herein, the micro-fracture is assumed as the grain abrasion and the fracture refers to the grain macro-fracture. Fracture happens as a consequence of tensile stresses induced into the abrasive grains. Besides the tangential grinding force F_t and the normal grinding force F_n, the force torque is also one of the mechanical loads result in stresses, as shown in Fig.4 (b-d). The AAG is supposed as a regular pyramid and the tangential grinding force is merely acted on grain cutting edge. Brittle fracture crack originates from the inner region where the maximum stress exists. Point A in Fig. 4(b) is the maximum stress concentration point which is verified by the FE simulation method (Fig. 4 (c-d)). The apex of an AAG is replaced by a very small plane. The element type used is SOLID45 and the mesh contains 2541 elements and 3024 nodes. The simulated normal force is 5.6 N obtained from the (85) in Section III.D. The tangential force is 2.8 N according to the empirical value of F_n/F_t presented by Zhou Zehua [29]. The normal and tangential force is loaded on the apex and side surface of the AAG within the interference depth region, respectively. The AAG stress distribution is analyzed by the first strength theory. In Fig.4 (b), the force torque M and stress σ in point A is determined with the normal and tangential forces.

$$M = F_t\,(h - h_{int}) + \int_{l_{min}}^{l_{max}} F_n l dl \tag{47}$$

$$l_{min} = \frac{a}{2} - h_{int} tan\frac{\alpha}{2} \tag{48}$$

$$l_{max} = \frac{a}{2} + h_{int} tan\frac{\alpha}{2} \tag{49}$$

$$\sigma = M/W \tag{50}$$

$$W = \frac{4}{3}\left(h_{int} tan\frac{\alpha}{2}\right)^3 \tag{51}$$

where W is the section modulus.

The bending strength of the alumina abrasive grains is approximately 290 MPa [30], [31]. Substituting (13) and (27) into (47-51), the macro-fracture occurs when the AAG protrusion height exceeds 135 μm. During the grinding process, the feeding motion is performed numerous. Although the AAG abrasion amount is gradually decreased along with the increasing of the feeding number, the change is small. Thus, the average value is used to define the AAG abrasion amount in this paper. The dressing and grinding experiments of the wheel are carried out and the statistical analysis results of abrasive grains protrusion height are written in table 3 by Kang *et al.* [27]. The AAG number within 110-160 μm after grinding is considerably reduced while it all have different increase amounts in the range of 80-90 μm, 90-100 μm, 100-110 μm and 110-120 μm. The average value of the increment of AAG number in each range after wear is shown in Fig.5 (a).

It is difficult to experimentally determine the amount of the abrasion wear or fracture wear of the AAG since it is impossible to track each AAG during the grinding process. Herein, the AAG wear amount is quantified through the probability assignment function and the DS (Dempster-Shafer) evidence theory. It is supposed that at least one abrasive particle in the subset is assigned to all subsets of the spaced grades. The distribution of the number of worn and broken AAGs in each height range is expressed in Fig.5 (c). And the corresponding AAG abrasion amount is calculated as below.

$$h^{100}_{abrasion} = \frac{\sum_{i=1}^{9} h^{100} - 95*5 - 88.5*4}{9N} \tag{52}$$

$$h^{110}_{abrasion} = \frac{\sum_{i=1}^{12} h^{110} - 105*4 - 95*7 - 88.5*1}{12N} \tag{53}$$

$$h^{120}_{abrasion} = \frac{\sum_{i=1}^{17} h^{120} - 115*4 - 105*11 - 95*1 - 88.5*1}{17N} \tag{54}$$

$$h^{135}_{abrasion} = \frac{\sum_{i=1}^{7} h^{135} - 115*4 - 105*1 - 95*1 - 88.5*1}{7N} \tag{55}$$

$$h^{140}_{fracture} = \frac{\sum_{i=1}^{7} h^{140} - 75*3 - 65*4}{7} \tag{56}$$

$$h^{150}_{fracture} = \frac{\sum_{i=1}^{7} h^{150} - 75*4 - 65*3}{7} \tag{57}$$

where $h^{100}_{abrasion}$, $h^{110}_{abrasion}$, $h^{120}_{abrasion}$, $h^{135}_{abrasion}$ are AAG abrasion amounts in the range of 90-100 μm, 100-110 μm, 110-120 μm, 120-135 μm, respectively in the single feeding motion. $h^{140}_{fracture}$, $h^{150}_{fracture}$ are AAG fracture amounts in the range of 135-140 μm and 140-150 μm, respectively. They are illustrated in Fig.5. (b).With the rising protrusion height of the AAG, it has an increase in its average abrasion amount. They are 0.0623 μm, 0.1628 μm, 0.2113 μm and 0.4496 μm, respectively. Especially, the AAG abrasion amount in 120-135 μm is more than twice that in 110-120 μm. The AAG abrasion results in a reduction of its protrusion height and the interference depth and the undeformed chip thickness size is inevitably declined. In addition, AAG exceeding 135 μm will not be able to participate in grinding due to the larger fracture amount (Fig.5. (b)). Therefore, a decrease is not only in the AAG density but in the MUCT size. Taking the AAG wear into account, the height h' of the AAG in each protruding height distribution interval is expressed by (58).

$$h' = \begin{cases} h - h^{100}_{abrasion}\ (h \in (90, 100\mu m]) \\ h - h^{110}_{abrasion}\ (h \in (100, 110\mu m]) \\ h - h^{120}_{abrasion}\ (h \in (110, 120\mu m]) \\ h - h^{135}_{abrasion}\ (h \in (120, 135\mu m]) \end{cases} \tag{58}$$

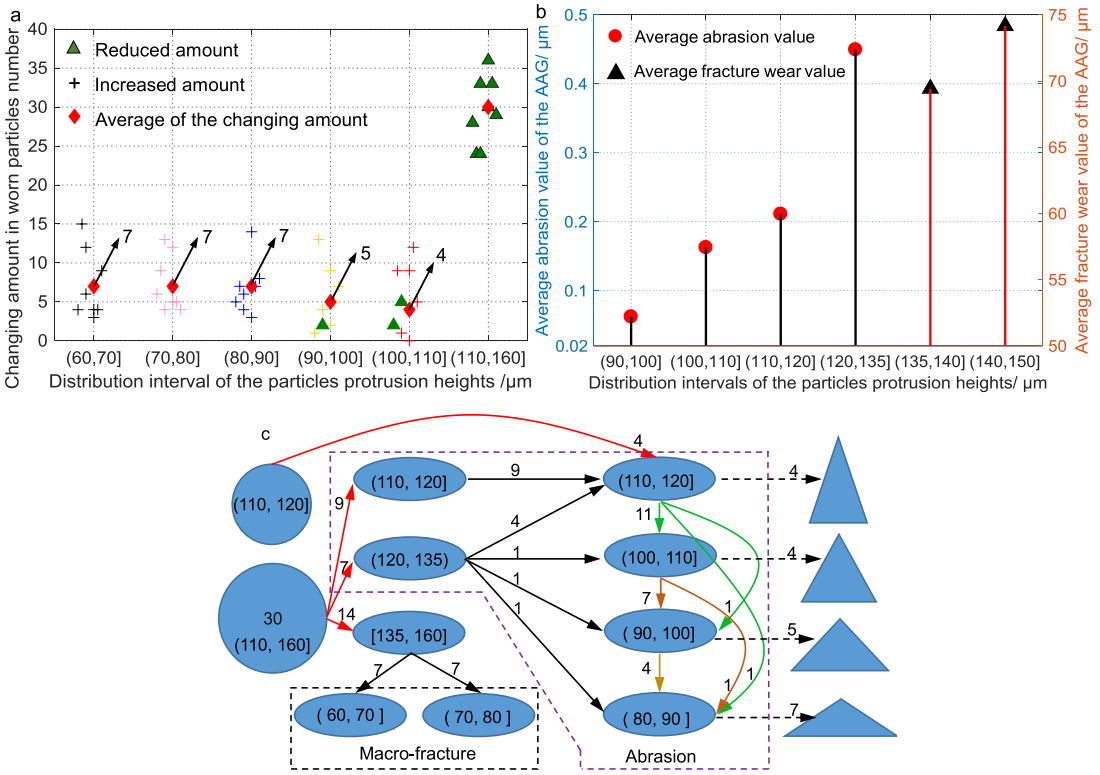

FIGURE 5. (a) The changing amount of the worn particles in different height distribution intervals; (b) The average abrasion or fracture wear value of the AAG in different height distribution intervals; (c) Distribution of the abrasive wear or fracture wear in each height distribution interval.

Substituting (58) into (16-40), the undeformed chip thickness models of a single AAG are as below.

$$h_{sum}^{\prime uct} = \int_{-rsin\theta_{na}'}^{0} \left(\sqrt{(r')^2 - x^2} - r'cos\theta_{na}'\right) \Big/ N dx + \int_{0}^{\theta_{na}} \left[r' - \left((r')^2 A^2\theta^2 + (r')^2 - 2(r')^2 A\theta^2\right)^{1/2} + h_{int}'\right] d\theta + \int_{\beta_0'}^{\beta_1'} \left(r' - \frac{d_s/2 + h_0 - ap}{sin\beta'}\right) d\beta' \quad (59)$$

$$\overline{h_{sum}^{\prime uct}} = r'\left(\frac{4 - \sqrt{1 - \theta_{na}^2/B} - cos\theta_{na}'/N}{6} - \frac{\sqrt{B}arcsin\left(\theta_{na}/\sqrt{B}\right)}{6\theta_{na}} + \frac{arccos\left(sin\theta_n'\right) - \pi/2}{6sin\theta_n' N}\right) + \frac{h_{int}'}{3} - \frac{6695ln\, sin\beta_0'/sin\beta_1'}{\beta_1' - \beta_0'} \quad (60)$$

$$h_{ti}^{\prime uct} = \left(r'' - \left((r')^2 A^2\theta_i^2 + (r')^2 - 2(r')^2 A\theta_i\left(\theta_{na}' + \theta_i\right)\right)^{1/2}\right) \Big/ N \times \left(\theta_i \in \left[-\theta_{na}', 0\right)\right) \quad (61)$$

$$h_{ti}^{\prime uct} = r' - \left((r')^2 A^2\theta_i^2 + (r')^2 - 2(r')^2 A\theta_i^2\right)^{1/2} + h_{int}' \left(\theta_i \in [0, \theta_{na}]\right) \quad (62)$$

$$h_{ti}^{\prime uct} = r' - \frac{d_s/2 + h_0 - ap}{sin\beta'} \left(\beta' \in \left[\beta_0', \beta_1'\right]\right) \quad (63)$$

$$r' = \frac{d_s}{2} + h' \quad (64)$$

$$cos\theta_{na}' = \frac{d_s/2 + h_0}{r'} \quad (65)$$

$$cos\theta_{na} = \frac{r' - ap - h_{int}'}{r'} \quad (66)$$

$$h_{int}' = \frac{h - h_0}{N} - h + h' \quad (67)$$

$$\beta_0' = arcsin\left(\frac{d_s/2 + h_0 - ap}{r' - h_{muct}'}\right) \quad (68)$$

$$\beta_1' = arcsin\left(\frac{d_s/2 + h_0 - ap}{r'}\right) \quad (69)$$

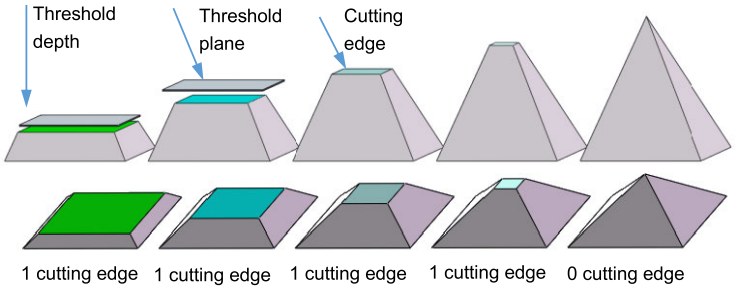

FIGURE 6. Cutting edge number with different threshold depths.

$$\beta' = arccos\frac{\left(r' - h_{ti}^{\prime uct}\right)^2 + \left(r'\right)^2 - \theta_i^2\left(r'\right)^2 A^2}{2r'\left(r' - h_{ti}^{\prime uct}\right)} + \frac{\pi}{2} - \theta_i \tag{70}$$

$$h'_{muct} = r' - \left(\left(r'\right)^2 A^2\theta_{na}^2 + \left(r'\right)^2 - 2\left(r'\right)^2 A\theta_{na}^2\right)^{1/2} + h'_{int} \tag{71}$$

were, the variables r', θ'_{na}, θ_{na}, h'_{int}, β'_0, β'_1, β', h'_{muct}, $h_{ti}^{\prime uct}$, $h_{sum}^{\prime uct}$, $\overline{h_{sum}^{\prime uct}}$ are values of the corresponding variables r, θ'_n, θ_n, h_{int}, β_0, β_1, β, h^{muct}, h_{ti}^{uct}, h_{sum}^{uct}, $\overline{h_{sum}^{uct}}$ after considering the AAG abrasion, respectively. Equations. (59-63, 71) are the sum of undeformed chip thickness, the average value and its value at any time in the first, second and third stages and the MUCT generated, respectively. It considers the real interference depth which is highly dependent on the protrusion height and abrasion of the AAG. Simultaneously, the chip width with AAG wear is in $[0.6a'h'_{UCT}/h', \sqrt{3.92}a'h'_{UCT}/h']$. Where $a' = 2h'tan\left(\alpha/2\right)$. Since chips are products of the interactions between the AAG tip and workpiece, its distribution and density are the same as those of the AAG. The investigation of the undeformed chip thickness distribution is carried out based on the AAG distribution and influences of the deformations in the wheel-workpiece and grain-workpiece contact regions.

D. DISTRIBUTION OF CHIPS

As demonstrated in Fig. 6, a threshold plane cuts through an AAG at different threshold depths. Only one cutting edge is produced when the threshold plane is in contact with the AAG, regardless of the threshold depth. Therefore, there is only one active cutting edge when the AAG contacts with the workpiece, and its density is equal to the AAG density. Active cutting edges' count N_{ace} is dependent on the contact area S_{cont} between the wheel and workpiece which is decided by the real contact arc length l_r and workpiece width $w_{workpiece}$.

$$N_{ace} = den_{AAG}S_{cont} \tag{72}$$

$$S_{cont} = l_r w_{workpiece} \tag{73}$$

The contact arc length generally includes three different definitions like geometry contact arc length, kinematic contact arc length and real contact arc length. Geometry contact arc length l_g refers to the length of the geometry grinding arc which incorporates the grinding depth effect and it is written as below [7].

$$l_g = \sqrt{a_p d_e} \tag{74}$$

where d_e is the wheel equivalent diameter with researches on grinding contact problems, the impact of motion parameters on the contact arc length is gradually recognized. Kinematic contact arc length is put forward. Actually, the phenomenon in the grinding region is quite complicated. In addition to deformations of elastic, plastic and heat, the abrasives' size, shape, and distribution have influences on the contact arc length. Therefore, the real contact arc length which can more accurately describe the impacts of the grinding mechanism and grinding parameters is presented. Concerning the difference from ordinary grinding wheels, a single symmetry plane of the shaped wheel is equally divided along the busbar direction according to the AAG density, as shown in Fig.7 (b). The number of equal parts n_p is

$$n_p = ceil\left(7 \times \sqrt{21}\right) \tag{75}$$

In Fig.7 (b), each portion is assumed as a cylinder since its small height, and its radius R_i is approximated by the mean value of the top and bottom radius r_i, r_{i+1} of each little truncated cone.

$$R_i = \left(r_i + r_{i+1}\right)/2\ (i = 1, 2, 3, \ldots, 33) \tag{76}$$

Stress is distributed throughout the wheel and the stress region is extremely large relative to the grain size. Thus, the wheel elastic behavior can be approximated by assuming it to be a continuum although it is a composite structure of grits, bond and voids [9], [32]. Ignoring AAG influences, the elastic deformation between the ith cylinder and the workpiece is exhibited in Fig.7 (c) according to the Hertz contact theory. The length of the contact region $2b_i$ is written below [33].

$$2b_i = \sqrt{\frac{16}{\pi}R_i\left(\frac{1-u_1^2}{E_1} + \frac{1-u_2^2}{E_2}\right)P_i} \tag{77}$$

where u_1, E_1 and u_2, E_2 are elasticity modulus and Poisson's ratio for the wheel and workpiece, respectively. P_i is the normal grinding force on the ith cylinder. According to

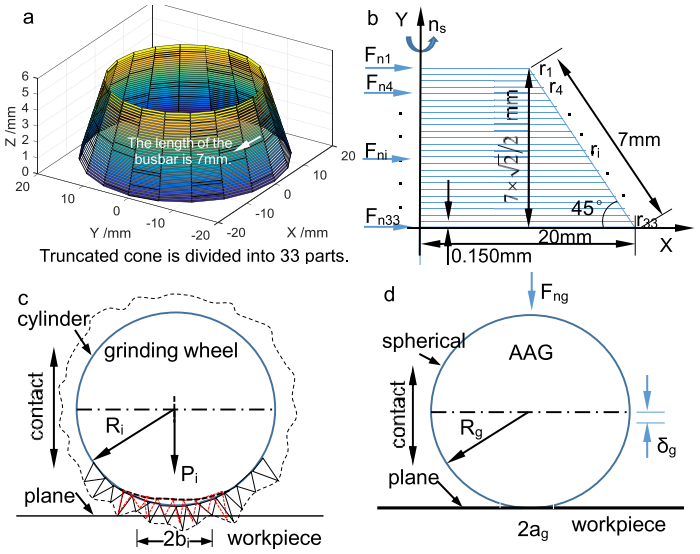

FIGURE 7. (a) Size of the shaped wheel in the raceway grinding region; (b) Force distribution; (c) Deflection within the wheel-workpiece contact zone; (d) Deflection within the AAG-workpiece contact zone.

Malkin model [31], [32], the normal grinding force per unit width is

$$F_{n'}^{Malkin} = \left(K_1 + K_2 \ln \frac{V_s^{1.5}}{a_p^{0.25} V_w^{0.5}}\right) \frac{V_w a_p}{V_s} + \frac{\gamma_0 V_w}{V_s} \left(\frac{a_p}{d_e}\right)^{1/2} \tag{78}$$

The linear velocity V_{si} of the forming wheel is not a constant value. It is closely related to the wheel radius.

$$V_{si} = 2\pi n_s r_i \ (i = 1, 2, 3, \ldots, 33) \tag{79}$$

where n_s is the rotating speed (rad/s). Substituting (79) into (78), the distributed force P_i is, (80) as shown at the bottom of this page, where K_1, K_2, γ_0 are coefficients determined by grinding experiments. Considering the deformation of the formed wheel, the AAG number N_d^i of the ith cylinder is written as (81) according to (72-73, 77).

$$N_d^i = \sqrt{\frac{8}{\pi}(r_i + r_{i+1}) \left(\frac{1-u_1^2}{E_1} + \frac{1-u_2^2}{E_2}\right) P_i \frac{w_{workpiece}}{n_p - 1}} \times den_{AAG} \quad (i = 1, 2, \ldots, 33) \tag{81}$$

Since the AAG is randomly distributed, it is assumed that the normal grinding force F_{ng} applied to each AAG is equal.

$$F_{ng} = \sqrt{P_i \Big/ \left(\frac{8}{\pi}(r_i + r_{i+1}) \left(\frac{1-u_1^2}{E_1} + \frac{1-u_2^2}{E_2}\right)\right) \Big/ \times \left(\frac{w_{workpiece}}{n_p - 1} den_{AAG}\right)} \quad (i = 1, 2, \ldots, 33) \tag{82}$$

The wheel shaft is vertically installed during the raceway grinding process, and the experimental test of the grinding force is difficult to develop. Herein, F_{ng} is approximately calculated by Xu *et al.* [2]. In combination with a relationship for the removal rate in scratching derived by Xu and Jahanmir [36], Xu *et al.* [2] approximated the volume of material removed V per unit sliding distance as

$$V = A_2 \left(E_w^{4/5} \Big/ Har^{9/5}\right) p^2 / T \tag{83}$$

where T is the fracture toughness. A_2 is a constant that may depend on the indenter geometry, sliding speed, etc., P is the normal force on the abrasive particle which is equal to F_{ng}. Ew is the elasticity modulus of the workpiece. Har is the Vickers hardness. By ignoring or rounding off some exponents, F_{ng} can be expressed as (85) through simplifying (84) [2].

$$F_{ng} = \beta_2 \left(T^{1/2} Har^{9/10} \Big/ E_w^{2/5}\right) (V_w / V_s)^{3/4} ap^{11/12} d_s^{1/12} \tag{84}$$

$$F_{ng} = \beta_2 \left(T^{1/2} Har \Big/ E_w^{2/5}\right) (V_w / V_s)^{3/4} ap \tag{85}$$

The constant β_2 is approximately equal to 0.85 [2]. After obtaining F_{ng}, the wheel contact deformation can be decided according to (77, 82, 85). Contact deflection also occurs within the abrasive-workpiece zone and it is calculated without considering that of the wheel. AAG is assumed as a spherical with radius R_g which is half of h. AAG is pressed against the workpiece surface under F_{ng}, as enunciated in Fig.7 (d).

$$P_i = 0.15 \int_{r_i}^{r_{i+1}} \frac{1.5K_2 V_w a_p (1 - \ln 2\pi nr) - K_1 V_w a_p - \gamma_0 V_w \sqrt{a_p / d_e} + K_2 V_w a_p ln\, a_p^{0.25} V_w^{0.5}}{r^2} dr \tag{80}$$

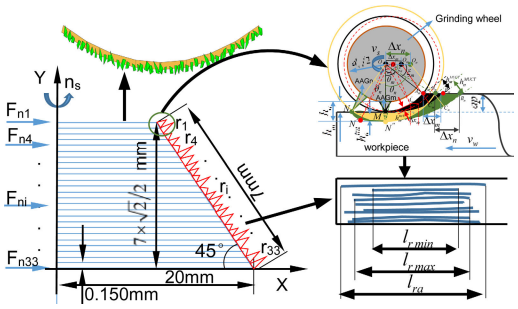

FIGURE 8. The geometry contact arc length generated by AAGs.

The deflection amount δ_g is given by Roark [37].

$$\delta_g = \sqrt[3]{\frac{9}{16R_g}\left(\frac{1-u_1^2}{E_1}+\frac{1-u_2^2}{E_2}\right)F_{ng}^2} \tag{86}$$

$$R_g = \frac{h}{2} \tag{87}$$

δ_g of the AAG is equivalent to an increase in the grinding depth and the contact arc length $2a_g$ caused by δ_g is written as

$$2a_g = \sqrt{d_e\delta_g} \tag{88}$$

Since the wheel radius is much larger than the contact arc length, the increment l_{in} in contact arc length can be given by the sum of contact lengths caused by deflections of the wheel and abrasives.

$$l_{in}^i \cong 2b_i + 2a_g \tag{89}$$

The real contact arc length is proposed by Rowe *et al.* [13], [38], [39] through incorporating the effect of grinding depth with the elastic deflection.

$$l_r^i = \left(\left(l_{in}^i\right)^2 + \left(l_g^i\right)^2\right)^{0.5} \quad (i = 1, 2, 3, \ldots, 33) \tag{90}$$

As presented in Fig.8, due to AAG' variable protrusion heights, the geometry contact arc length generated is different. It contains the maximum contact arc length $l_{r\,max}$, minimum contact arc length $l_{r\,min}$ and arbitrary contact arc length l_{ra}. From the chip generation mechanism in Fig.2, the AAG cutting path length is approximately equal to the contact arc length, which is verified by Malkin [3], [7]. Accordingly, the real geometry contact arc length of the n th AAG on the ith little truncated cone is calculated as (91) after considering the influences of the grinding depth and the AAG protruding height on the interference depth.

$$l_{gri}^n = NN'' + N''B_n \tag{91}$$

$$NN'' = \theta_n'\left(d_{si}/2 + h_{int}^n\right) \tag{92}$$

$$NN''B_n = \sqrt{\left(h_{int}^n + ap\right)d_{ei}^n} \tag{93}$$

$$l_{gri}^n = \sqrt{\left(h_{int}^n + ap\right)d_{ei}^n} + \theta_n'\left(d_{si}/2 + h_{int}^n\right) \tag{94}$$

Considering the AAG wear,

$$l_{gri}'^n = \sqrt{\left(h_{int}'^n + ap\right)d_{ei}^n} + \theta_n'\left(d_{si}/2 + h_{int}'^n\right) \tag{95}$$

For straight grinding, $d_{ei} = d_{si}$, thus, $d_{ei}^n = d_{si}$. Substituting (76-77, 86-90, 95) into (90), the real contact arc length value of the n th AAG is expressed as

$$\begin{aligned} l_{ri}^n = &\left(\frac{8}{\pi}\left(r_i + r_{i+1}\right)WP_i + d_{si}\delta_{gi}^n\right. \\ &+ \frac{8}{\sqrt{\pi}}\left(W\delta_{gi}^n d_{si}\frac{r_i + r_{i+1}}{2}P_i\right)^{1/2} + \left(h_{int}'^n + ap\right)d_{si} \\ &+ \left(\theta_n'\left(d_{si}/2 + h_{int}'^n\right)\right)^2 + 2\theta_n'\left(d_{si}/2 + h_{int}'^n\right) \\ &\left.\times\sqrt{\left(h_{int}'^n + ap\right)d_{si}}\right)^{1/2} \quad (i = 1, 2, \ldots, 33) \end{aligned} \tag{96}$$

$$\begin{aligned} l_{ri}^n = &\left(\frac{8}{\pi}\left(r_i + r_{i+1}\right)WP_i + d_{si}\delta_{gi}^n\right. \\ &\left.+ \frac{8}{\sqrt{\pi}}\left(W\delta_{gi}^n d_{si}\frac{r_i + r_{i+1}}{2}P_i\right)^{1/2} + \left(h_{int}'^n + ap\right)d_{si}\right)^{1/2} \\ &\times (i = 1, 2, \ldots, 33) \end{aligned} \tag{97}$$

Since θ_n' is very small, the contribution of $\theta_n'\left(d_{si}/2 + h_{int}'^n\right)$ to the total length l_{ri}^n may be negligible, in which case, l_{ri}^n is simplified into (97). Where $W = \frac{1-u_1^2}{E_1} + \frac{1-u_2^2}{E_2}$. After obtaining the real contact arc length, the AAG distribution and number in the grinding area is determined. Combined with the undeformed chip thickness model of a single AAG, the distribution model of the average undeformed chip thickness or MUCT can be established.

IV. MODEL SIMULATIONS

After establishing models of the real contact arc length, active cutting edge, MUCT and mean undeformed chip thickness the corresponding simulations are performed with wheel dressing and grinding experiments results provided by Kang *et al.* [27]. The grinding process parameters and experimental results are written in table 2.

A. SIMULATIONS OF A SINGLE UNDEFORMED CHIP THICKNESS

Fig.9 (a) is the simulation results of three stages of an entire chip generated by a single AAG with different protrusion heights. Since the higher AAG has a greater interference depth, the average undeformed chip thickness and the MUCT are raised with the enlarged AAG protrusion height. Whereas, it has varying degrees decline when the AAG wear is in consideration (Fig.9 (b)). Moreover, there is no chip generated when the AAG is larger than 135 μm since the AAG could not participate in grinding due to the fracture wear. Contact arc length of the AAG with typical five different protrusion heights by considering different affecting factors is expressed in Fig.9 (c). Relative to the constant value l_g, l_{gr} is increased with the rising AAG protrusion height

TABLE 2. The grinding process parameters and wheel experimental results.

u_1	u_2	$w_{workpiece}$ (mm)	den_{AAG} (mm^2)	Vw (m / min)	Vs (m / s)	ap (μm)
0.266	0.3	7	21	22	30	2
E_1 (GPa)	E_2 (GPa)	*grinding amount*	$d_e = d_s$ (mm)	F_n (N)	F_t (N)	h_0 (μm)
373	207	0.1 mm	(30,40]	5.6	2.8	87
β_2	T (MPa)	$h^{100}_{abrasion}$ (μm)	$h^{110}_{abrasion}$ (μm)	$h^{120}_{abrasion}$ (μm)	$h^{135}_{abrasion}$ (μm)	*Har*
0.85	290	0.0623	0.1628	0.2113	0.4496	640

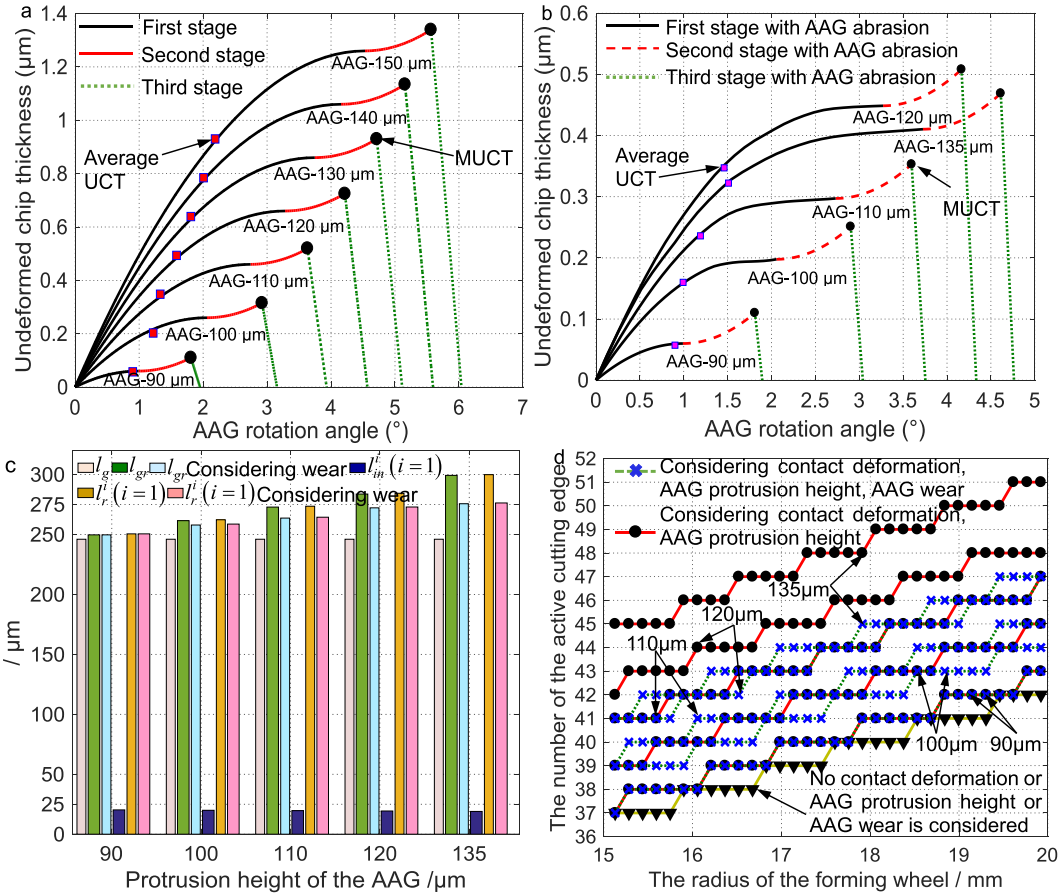

FIGURE 9. (a) The entire chip produced by a single AAG; (b) The produced entire chip considering AAG wear; (c) Comparison between the geometry contact arc length and the real contact arc length; (d) Active cutting edges' number with different influencing factors.

while l_{gr} is decreased when AAG wear is considered and the gap gradually increases. Simultaneously, this difference is also reflected in true contact arc length with and without AAG wear. However, the contact arc length increment l^i_{in} caused by contact deformations is hardly changed. This illustrates that the AAG protrusion height and wear exert a greater effect on the real contact arc length than contact deformations. Number of the active cutting edges with different wheel radius and affecting factors is presented in Fig.9 (d). Since the contact area is expanded by the rising contact arc length resulted from the enlarged AAG protrusion height and the contact deformations, the active cutting edges' number is increased when thinking over these factors. Conversely, the active cutting edges' number is dropped as AAG wear reduces the contact area.

B. SIMULATIONS OF THE MEAN UNDEFORMED CHIP THICKNESS AND MUCT DISTRIBUTION

With the dressing and grinding experiments of the wheel conducted in the previous work [27], the probability density distribution histograms of abrasive grains' apex angle, width, and height are expressed in Fig.10. The specific AAG number and its distribution of the protrusion height can be determined through the contact arc length, active cutting edges' number.

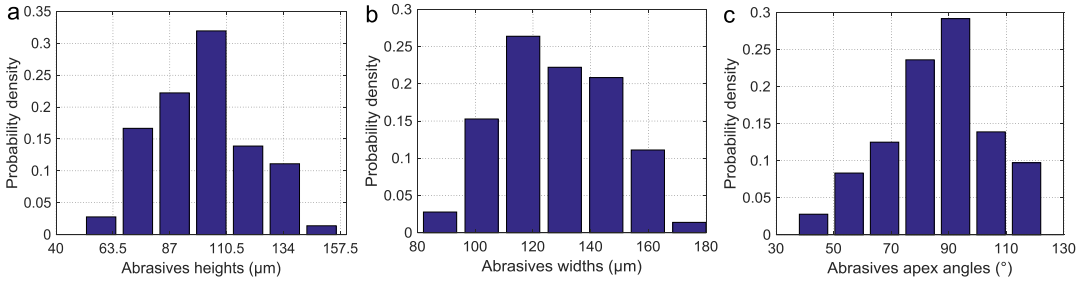

FIGURE 10. Probability density distribution histograms of abrasive grains' apex angle, width and height.

Combined with the undeformed chip thickness model of a single AAG, the simulated mean undeformed chip thickness and MUCT distribution in the entire grinding contact area are described in Fig.11.

In Fig. 11, the legends of 'AAG protrusion height', 'no wear' and 'with wear' refer to considering the AAG protrusion height, the AAG protrusion height and contact deformations, and three affecting elements, respectively. From Fig.11 (a, d), the frequency of the mean undeformed chip thickness or MUCT in all distribution intervals considering contact deformations is higher than that of only thinking the AAG protrusion height. Although the AAG wear is in consideration (Fig.11 (b, e)), it has the same variation. This indicates that the density of active cutting edges is enhanced by contact deformations while AAG wear has little impact on it. Whereas, the mean undeformed chip thickness value is decreased when AAG wear is in view and its distribution is mainly concentrated in 0.014-0.479 μm (Fig. 11 (b)). With increasing of the mean undeformed chip thickness value, its frequency goes from nearly twice to gradually lower than that of only thinking the AAG protrusion height. This change also occurs in the distribution of MUCT, as expressed in Fig.11 (e-f). MUCT distribution intervals are reduced to 0.046-0.539 μm from 0.046-1.032 μm. This demonstrates that AAG wear is the primary affecting factor on the value of MUCT or mean undeformed chip thickness values, especially in terms of hindering larger values. From Fig.11 (g-i), the frequency or probability of the average undeformed chip thickness is much higher than MUCT in the lower distribution range. And there is only MUCT when the distribution range exceeds a certain value which is called cut-off value in this paper. Comparing Fig. 11 (h) and Fig. 11 (g, i), the cut-off value is 0.293 μm when AAG wear is concerned and the maximum value of MUCT is 0.571 μm while it can be up to 0.693 μm without AAG wear, regardless of contact deformations and the MUCT is up to 1.031 μm. Simultaneously, AAG wear also has a great effect on the chip width that its maximum value is significantly descended, as presented in Fig.11 (j).

In addition, comparing (60, 71, 72, 91) and (1,2,3,74), undeformed chip thickness, MUCT, contact arc length, and active cutting edges are all fixed values and the value of MUCT is equal to undeformed chip thickness when the real interference depth of the AAG is not concerned. This is inconsistent with the actual situation. Accordingly, the simulated average undeformed chip thickness or MUCT value or distribution considering contact deformation and AAG wear is closer to the real situation based on the true interference depth of AAG. And the grinding experiments are carried out to verify the correctness and validity of the models.

V. EXPERIMENTS, RESULTS AND DISCUSSION

Grinding experiments of the slider raceway are performed by the single factor trial method, as shown in Fig.12. Four identical sliders are simultaneously ground, which can not only reduce experimental errors but also be used as repeated experiments. The specific grinding process parameters are in table 3. The raceway surface topography is measured by the Rtec dual-mode 3D topography instrument (UP, America) (Fig.13). Fig. 13 (a-d) are the 3D topographies of the slider raceway surface when the feeding rate is 25 m/min, the wheel linear speed is 30 m/s, and the grinding depths are 2 μm, 5 μm, 8 μm and 11 μm, respectively. From the size and distribution of grooves and protrusions, it can be seen that the height difference between grooves and protrusions is enlarged, and the width of grooves is also raised with the increase of the grinding depth. The 3D morphologies of the slider raceway surface when the feed speed is 25 m/min, grinding depth is 5 μm, and the wheel linear speeds is 15 m/s, 20 m/s, 30 m/s and 40 m/s are given as Fig. 13 (e-h), respectively. With an increase in the wheel linear speed, the distribution of grooves and protrusions is more uniform and the height difference becomes smaller. Thus, the surface quality is improved. However, the height difference between the groove and the protrusion in the surface topography becomes larger and the uniformity of its distribution is worse with the rising of the workpiece feeding speed when the linear speed of the grinding wheel is 30 m/s and the grinding depth is 5 μm. The surface quality is deteriorated and the corresponding 3D topographies of the slider raceway surface of the workpiece obtained with different feed speeds are shown in Fig.13 (i-l), respectively.

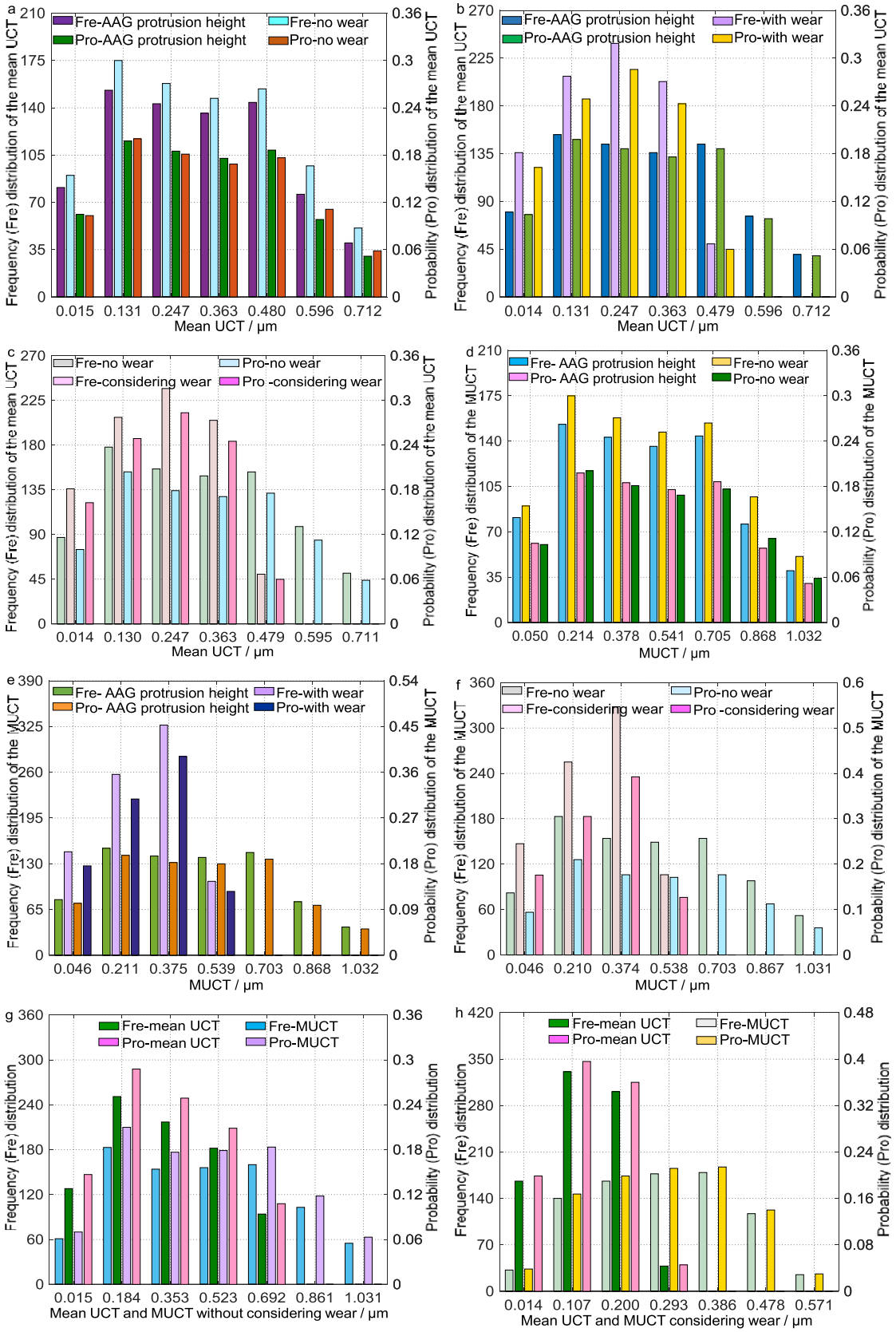

FIGURE 11. Distribution of the mean undeformed chip thickness (mean UCT) with (a) A and A, B; (b) A and A, B, C; (c) A, B and A, B, C; Distribution of MUCT with (d) A and A, B; (e) A and A, B, C; (f) A, B and A, B, C; Distribution of the mean undeformed chip thickness and MUCT with (g) A and B; (h) A, B and C; (i) A; (j) Distribution of the minimum and maximum chip width with A and A, B. Where, A is the AAG protrusion height, B is the contact deformation and C is the AAG wear.

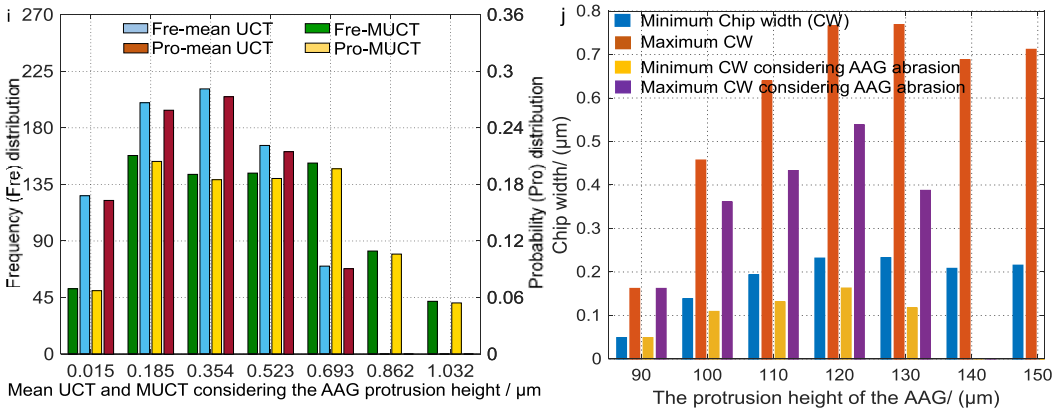

FIGURE 11. ***(Continued.)*** **Distribution of the mean undeformed chip thickness (mean UCT) with (a) A and A, B; (b) A and A, B, C; (c) A, B and A, B, C; Distribution of MUCT with (d) A and A, B; (e) A and A, B, C; (f) A, B and A, B, C; Distribution of the mean undeformed chip thickness and MUCT with (g) A and B; (h) A, B and C; (i) A; (j) Distribution of the minimum and maximum chip width with A and A, B. Where, A is the AAG protrusion height, B is the contact deformation and C is the AAG wear.**

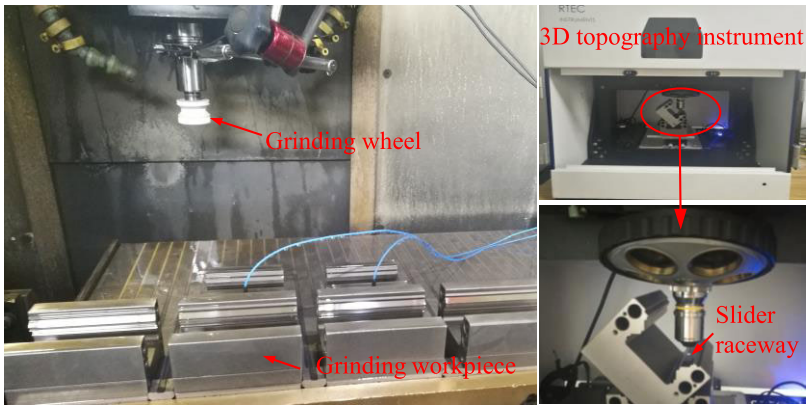

FIGURE 12. **Slider grinder *PLANMATHP 408* and 3D topography instrument.**

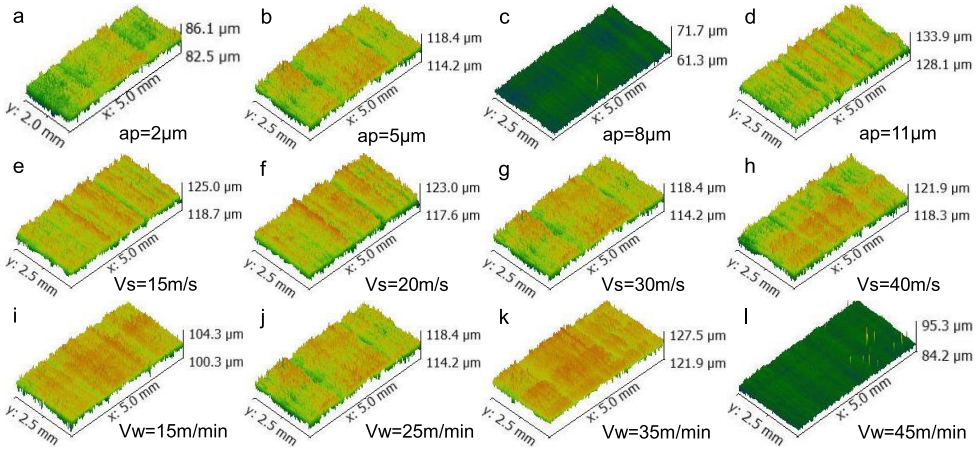

FIGURE 13. **Surface topographies: (a-d) $Vw = 25$ m/min, $Vs = 30$ m/s; (e-h) $Vw = 25$ m/min, $ap = 5\mu$m; (i-l) $Vs = 30$ m/s, $ap = 5\mu$m.**

Material removal is accompanied by chip formation and its cumulative effect is the generation of the grooves and protrusions in the surface which can be approximated by the MUCT distribution in the grinding direction, as described in Fig 1.(g, h). Herein, the MUCT distribution model is utilized to predict the surface roughness and the model's

TABLE 3. Specific experimental parameters, samples and equipment.

No.	*Vw* (m / min)	*Vs* (m / s)	*ap* (μm)	Experimental samples and equipment	
1	25	30	2	Grinding workpiece	GZB45BA
2	25	30	8		
3	25	30	11	Material	GCr15
4	25	15	5	Wheel	$1A46\times25\times13-SA100K-35$
5	25	20	5	Material	Alumina
6	25	40	5	Slider grinder	$PLANMATHP408$
7	15	30	5		
8	35	30	5	Grinding fluid	Fully synthetic water-soluble cutting fluid
9	45	30	5		
10	25	30	5		

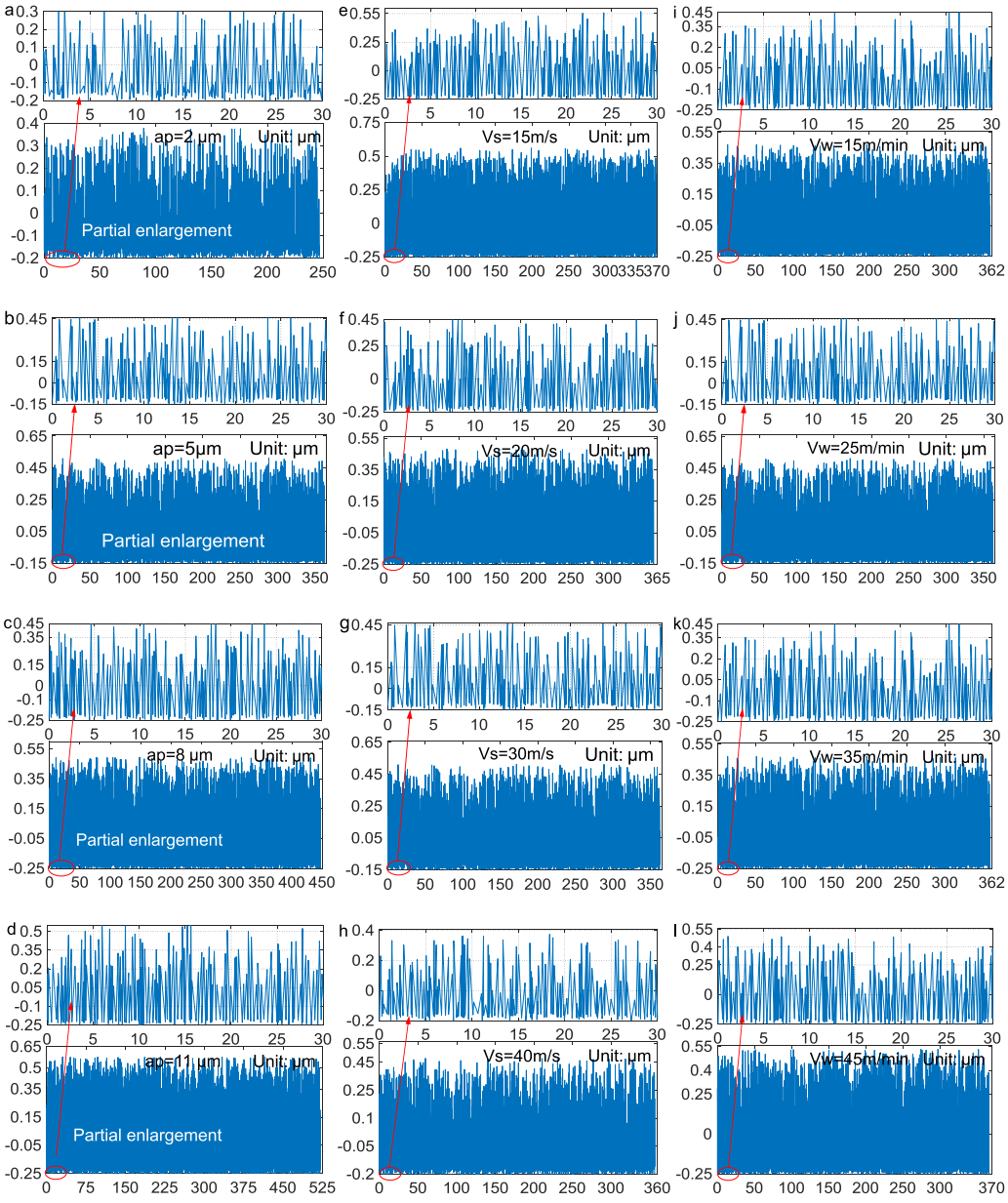

FIGURE 14. Simulated surface roughness profiles of the slider raceway: (a-d) Vw = 25 m/min, Vs = 30 m/s; (e-h) Vw = 25 m/min, ap = 5μm; (i-l) Vs = 30 m/s, ap = 5μm.

correctness is verified through the comparison of the predicted and experimental roughness. The surface roughness is characterized by parameters Ra which is only related to the size of MUCT rather than its distribution position, as illustrated in (98). The surface contour can be formed after obtaining the distribution probability of the MUCT height and

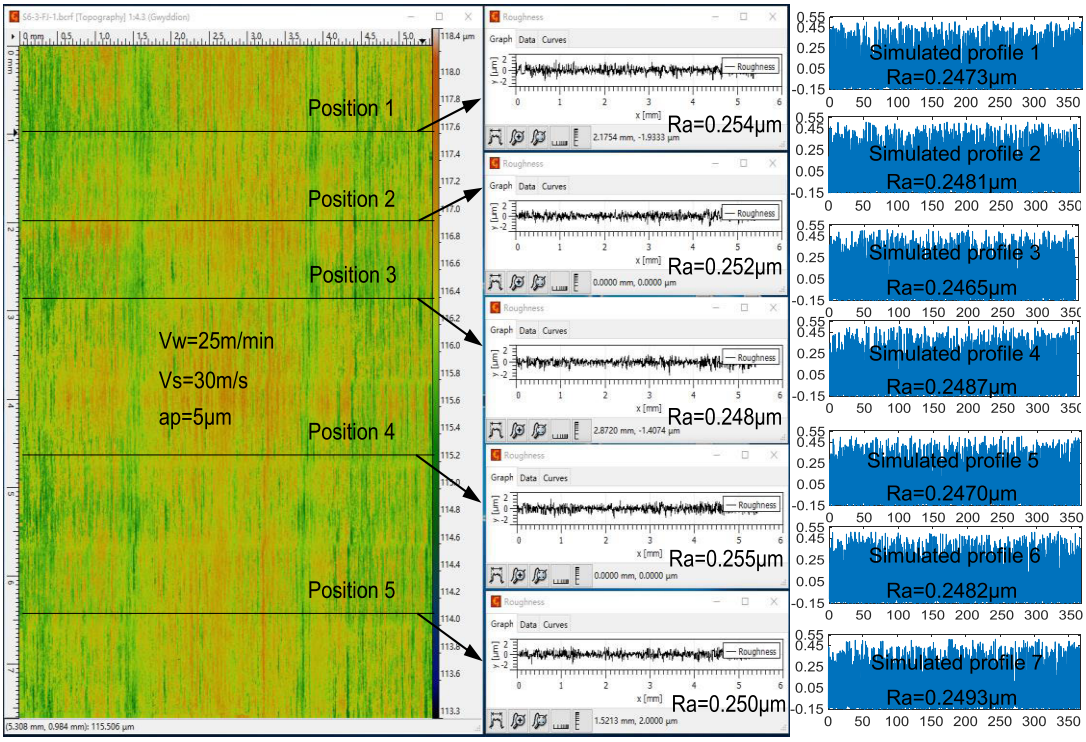

FIGURE 15. **Methods for determining the experimental and simulated values of Ra.**

width, as shown in Fig.14.

$$
\begin{aligned}
&Ra_{profile} \\
&= f\left(\left[\left\{h^1_{MUCT}, w^1_{MUCT}\right\}, \left\{h^2_{MUCT}, w^2_{MUCT}\right\}, \ldots,\right.\right. \\
&\quad \left.\left.\left\{h^n_{MUCT}, w^n_{MUCT}\right\}\right]\right) \\
&= f\left(\left[\left\{h^{random1}_{MUCT}, w^{random1}_{MUCT}\right\}, \left\{h^{random2}_{MUCT}, w^{random2}_{MUCT}\right\}, \ldots,\right.\right. \\
&\quad \left.\left.\left\{h^{randomn}_{MUCT}, w^{randomn}_{MUCT}\right\}\right]\right) \qquad (98)
\end{aligned}
$$

The simulated roughness profiles of the slider raceway surface take into account all the influencing factors including AAG protrusion height, contact deformations and AAG wear. From the partially enlarged views in Fig. 14 (a-d), it can be observed that the maximum value of roughness is increased from 0.3 μm to 0.5 μm, and the uniformity of profiles becomes worse with the increase of grinding depth. Consequently, the surface quality is deteriorated. However, the surface quality is enhanced with the rising of the linear velocity, as shown in Fig. 14 (e-h). The maximum value of roughness is decreased from 0.55 μm to 0.4 μm, and the number of the peaks and pits in the profile distribution is obviously reduced. With the raising of the workpiece feed speed, the increase in roughness value is not large, but the distribution of convex peaks and grooves in the profile becomes worse, the surface quality is worse as expressed in Fig. 14 (i-l). Then, the roughness values obtained through experiments and simulations are compared to verify the correctness of the MUCT model and the mean UCT model. The specific type of the slider is GRB45ZB (manufactured by Nanjing Yigong Co., Ltd.) in this paper. The width and length of the slider raceway is 7 mm and 106 mm, respectively. Since the feed direction of the slider is parallel to its length direction, the roughness in the width direction of the raceway is utilized to characterize its surface quality. As presented in Fig.15, in order to ensure the accuracy of experimental test values, the experimental roughness value is determined by the average of measurement values at five different positions with a width of 6mm during model validation. Similarly, the simulated contour is repeated 7 times and the average value of its roughness values is invoked as the predicted value. The comparison results are shown in Fig. 16.

It can be obviously seen from Fig. 16 that Ra is increased with the enlargement of grinding depths and the feed speed, and decreased with the rising linear speed. Moreover, the simulated values of Ra obtained from the MUCT model A that only considers AAG's protrusion height or model B thinking the AAG protrusion height and contact deformation are much larger than the experimental values of Ra. Whereas, the simulated values of Ra derived from the MUCT model C are very close to the experimental values of Ra. It concerns all influencing factors including the height of AAG protrusion, the contact deformations, and the AAG wear. It is illustrated that the influence of AAG's wear on MUCT is greater than the effect of AAG protrusion height and contact deformations within the wheel-workpiece and AAG-workpiece regions.

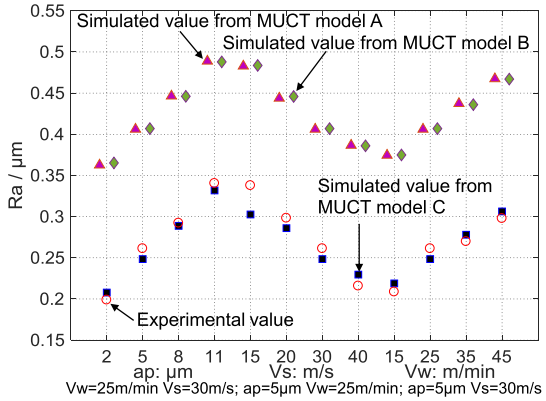

FIGURE 16. Comparison of the experimental and predicted roughness: Model A only considers the AAG protrusion height; Model B considers the AAG protrusion height and contact deformations; Model C considers the AAG protrusion height, contact deformations and the AAG wear.

In summary, the correctness and effectiveness of the MUCT distribution model obtained based on the real interference depth of the AAG that considering AAG protrusion height, AAG wear and contact deformations are verified.

VI. CONCLUSIONS

MUCT distribution model is established from the perspective of the real interference depth of the AAG according to the MUCT generated by a single AAG and the AAG distribution in the grinding area. The chip thickness and width of a single AAG are primarily determined through the kinematic analysis of the real interference depth. And the real AAG distribution is obtained after integrating the true contact arc length and active cutting edges' amount affected by the contact deformations with the AAG probability density distribution obtained from the wheel surface topography. The correctness and rationality of the MUCT distribution model are verified by the comparison of the predicted values and experimental values of the roughness. The key findings can be summarized as follows:

(1) The real interference depth of an AAG is the main factor that determines the MUCT size. It is highly dependent on the protrusion height and wear amount of the AAG. It is increased with the rising AAG protruding height and it has a different degree of decline when considering AAG wear.

(2) The AAG wear amount is greatly influenced by the AAG protrusion height in case of constant grinding forces, wheel binder, process parameters, etc. It is enlarged with the raising of the AAG protruding height and the fracture of an AAG occurs when its protrusion height exceeds 135 μm.

(3) The distribution of the MUCT is mainly decided by the probability density distribution of the AAG in the current grinding area. It is decided by the actual contact arc length and active cutting edges' number primarily affected by the contact deformation in the wheel-workpiece and AAG-workpiece region.

(4) The roughness profile simulated by the MUCT distribution model can be utilized to predict the roughness of the grinding surface. Moreover, the MUCT distribution model can lay the foundation for the study of 3D topography and surface integrity of the grinding surface.

ACKNOWLEDGMENT

The authors gratefully acknowledge Prof. Xing-Yan and Dr. Minghui-Pan for useful discussions and consultations, and PM Lingxiang-Yin who performed the grinding experiments.

REFERENCES

[1] M. C. Shaw, *Principles of Abtasive Processing*. New York, NY, USA: Oxford Univ. Press, 1996, pp. 57–80.
[2] H. Xu, S. Jahanmir, and L. K. Ives, "Mechanisms of material removal in abrasive machining of ceramics," *Interceram*, vol. 47, no. 6, pp. 380–386, Mar. 1998.
[3] S. Malkin and C. Guo, *Grinding Technology: Theory and Applications of Machining with Abrasives*, 2nd ed. New York, NY, USA: Industrial Press, 2008, pp. 39–51.
[4] D. Axinte, P. Butler-Smith, C. Akgun, and K. Kolluru, "On the influence of single grit micro-geometry on grinding behavior of ductile and brittle materials," *Int. J. Mach. Tools Manuf.*, vol. 74, pp. 12–18, Nov. 2013, doi: 10.1016/j.ijmachtools.2013.06.002.
[5] C. Dai, W. Ding, J. Xu, Y. Fu, and T. Yu, "Influence of grain wear on material removal behavior during grinding nickel-based superalloy with a single diamond grain," *Int. J. Mach. Tools Manuf.*, vol. 113, pp. 49–58, Feb. 2017, doi: 10.1016/j.ijmachtools.2016.12.001.
[6] S. C. Paolinelli, M. A. Cunha, and A. B. Cota, "Effect of hot band grain size on the texture evolution of 2% Si non-oriented steel during final annealing," *IEEE Trans. Magn.*, vol. 51, no. 6, pp. 1–4, Jun. 2015, doi: 10.1109/tmag.2014.2381155.
[7] W. B. Rowe, "Grinding technology-theory and applications of machining with abrasives," *Tribol. Int.*, vol. 23, no. 6, p. 443, Dec. 1990.
[8] L. R. Hecker and Y. S. Liang, "Predictive modeling of surface roughness in grinding," *Int. J. Mach. Tool Manu.*, vol. 43, no. 8, pp. 755–761, Jun. 2003, doi: 10.1016/S0890-6955(03)00055-5.
[9] S. Agarwal and P. V. Rao, "Predictive modeling of undeformed chip thickness in ceramic grinding," *Int. J. Mach. Tools Manuf.*, vol. 56, pp. 59–68, May 2012, doi: 10.1016/j.ijmachtools.2012.01.003.
[10] Y. Zhang, C. Fang, G. Huang, and X. Xu, "Modeling and simulation of the distribution of undeformed chip thicknesses in surface grinding," *Int. J. Mach. Tools Manuf.*, vol. 127, pp. 14–27, Apr. 2018, doi: 10.1016/j.ijmachtools.2018.01.002.
[11] X. Li, S. Wolf, G. Zhi, and Y. Rong, "The modelling and experimental verification of the grinding wheel topographical properties based on the 'through-the-process' method," *Int. J. Adv. Manuf. Technol.*, vol. 70, nos. 1–4, pp. 649–659, Sep. 2014, doi: 10.1007/s00170-013-5301-6.
[12] S. Wang, C. Li, D. Zhang, D. Jia, and Y. Zhang, "Modeling the operation of a common grinding wheel with nanoparticle jet flow minimal quantity lubrication," *Int. J. Adv. Manuf. Technol.*, vol. 74, nos. 5–8, pp. 835–850, Jun. 2014, doi: 10.1007/s00170-014-6032-z.
[13] W. B. Rowe, M. N. Morgan, H. S. Qi, and H. W. Zheng, "The effect of deformation on the contact area in grinding," *CIRP Manuf. Technol.*, vol. 42, no. 1, pp. 409–412 1993, doi: 10.1016/S0007-8506(07)62473-1.
[14] S. Y. Luo, "Characteristics of diamond sawblade wear in sawing," *Int. J. Mach. Tools Manuf.*, vol. 36, no. 6, pp. 661–672 Jun. 1996, doi: 10.1016/0890-6955(95)00071-2.
[15] R. Gahlin and S. Jacobson, "The particle size effect in abrasion studied by controlled abrasive surfaces," *Wear*, vol. 224, no. 1, pp. 118–125 Jan. 1999, doi: 10.1016/s0043-1648(98)00344-5.
[16] U. M. Bhatt, A. Kumar, and S. K. Manhas, "Performance enhancement by optimization of poly grain size and channel thickness in a vertical channel 3-D NAND flash memory," *IEEE Trans. Electron Devices*, vol. 65, no. 5, pp. 1781–1786, May 2018.
[17] W. Ding, Y. Zhu, L. Zhang, J. Xu, Y. Fu, W. Liu, and C. Yang, "Stress characteristics and fracture wear of brazed CBN grains in monolayer grinding wheels," *Wear*, vols. 332–333, pp. 800–809, May/Jun. 2015, doi: 10.1016/j.wear.2014.12.008.

[18] T. Zhou, K. Cher, J. F. Hu, and Z. Yuan, "Control of grain shape and size in FePt–TiO_2 nanocomposite thin films via artificial nucleation layers," *IEEE Trans. Magn.*, vol. 50, no. 11, pp. 1–4, Nov. 2014, Art no. 2302504.
[19] Q. Miao, W. F. Ding, J. H. Xu, C. Y. Yang, and Y. C. Fu, "Fractal analysis of wear topography of brazed polycrystalline cBN abrasive grains during grinding nickel super alloy," *Int. J. Adv. Manuf. Technol.*, vol. 68, nos. 9–12, pp. 2229–2236, Oct. 2013, doi: 10.1007/s00170-013-4823-2.
[20] S. Buhl, C. Leinenbach, R. Spolenak, and K. Wegener, "Failure mechanisms and cutting characteristics of brazed single diamond grains," *Int. J. Adv. Manuf. Technol.*, vol. 66, nos. 5–8, pp. 775–786, Jul. 2012, doi: 10.1007/s00170-012-4365-z.
[21] H. Wu, H. Huang, F. Jiang, and X. Xu, "Mechanical wear of different crystallographic orientations for single abrasive diamond scratching on Ta12W," *Int. J. Refractory Met. Hard Mater.*, vol. 54, pp. 260–269, Jan. 2016, doi: 10.1016/j.ijrmhm.2015.07.038.
[22] J. Y. Shen, J. Q. Wang, B. Jiang, and X. P. Xu, "Study on wear of diamond wheel in ultrasonic vibration-assisted grinding ceramic," *Wear*, vols. 332–333, pp. 788–793, May/Jun. 2015, doi: 10.1016/j.wear.2015.02.047.
[23] K. Ding, Y. Fu, H. Su, X. Gong, and K. Wu, "Wear of diamond grinding wheel in ultrasonic vibration-assisted grinding of silicon carbide," *Int. J. Adv. Manuf. Technol.*, vol. 71, nos. 9–12, pp. 1929–1938, Jan. 2014, doi: 10.1007/s00170-014-5625-x.
[24] W. F. Ding, Q. Miao, J. H. Xu, C. Y. Ma, B. Zhao, and C. Y. Yang, "Joining interface and grain fracture of single-layer brazed grinding wheels with binderless CBN grains," *Int. J. Adv. Manuf. Technol.*, vol. 68, nos. 5–8, pp. 1261–1266, Sep. 2013, doi: 10.1007/s00170-013-4917-x.
[25] M. D Acunto, "Theoretical approach for the quantification of wear mechanisms on the nanoscale," *Nanotechnology*, vol. 15, no. 7, pp. 795–801, Jul. 2004, doi: 10.1088/0957-4484/15/7/014.
[26] J. E. Fernández, M. R. Fernández, R. Vijande, and R. T. Navarro, "Abrasive wear analysis using factorial experiment design," *Wear*, vol. 255, nos. 1–6, pp. 38–43, Aug./Sep. 2003, doi: 10.1016/s0043-1648(03)00103-0.
[27] M. Kang, L. Zhang, and W. Tang, "Study on three-dimensional topography modeling of the grinding wheel with image processing techniques," *Int. J. Mech. Sci.*, vol. 167, Feb. 2020, Art. no. 105241, doi: 10.1016/j.ijmecsci.2019.105241.
[28] S. Spuzic, M. Zec, K. Abhary, R. Ghomashchi, and I. Reid, "Fractional design of experiments applied to a wear simulation," *Wear*, vol. 212, no. 1, pp. 131–139 Nov. 1997, doi: 10.1016/s0043-1648(97)00089-6.
[29] *'Metal Cutting Principle' in Grinding*, Nanjing Inst. Technol., Fujian Sci. Technol. Press, Fujian, China, 1984, pp. 1116–1121.
[30] J. Yaoy, T. Qiu, X. Jiang, and C. Li, "Modifying the bending strength and microstructure of alumina ceramics," *Electron. Compon. Mater.*, vol. 28, no. 6, pp. 1–3, Jun. 2009, doi: 10.3969/j.issn.1001-2028.2009.06.001.
[31] D. Yinsen, "Effect of Zirconia fiber on thermal shock resistance of alumina ceramics," Ph.D. dissertation, Jinan Univ., Jinan, China, 2012, doi: 10.7666/d.y2129274.
[32] R. H. Brown, K. Saito, and M. C. Shaw, "Local elastic deflections in grinding," *Ann. CIRP*, vol. 19, no. 1, pp. 105–113. Oct. 1971, doi: 10.1016/s0007-8506(07)61320-1.
[33] S. Timishenko and J. N. Goodier. *Theory of Elasticity*. New York, NY, USA: McGraw-Hill, 1951, pp. 375–390.
[34] Y. P. Chen, "Modeling of plane grinding force and its application," M.S. thesis, Central South Univ., Changsha, China, 2007.
[35] S. Malkin and N. H. Cook, "The wear of grinding wheels: Part 2—Fracture wear," *J. Eng. Ind.*, vol. 93, no. 4, pp. 1129–1133, Nov. 1971, doi: 10.1115/1.3428052.
[36] S. Jahanmir, H. H. K. Xu, and L. K. Ives, "Mechanisms of material removal in abrasive machining of ceramics," in *Machining of Ceramics and Composites*, S. Jahanmir, M. Ramulu, and P. Koshy, Eds. New York, NY, USA: Marcel Dekker, 1999, pp. 11–84.
[37] R. J. Roark, *Formula for Stress and Strain*. New York, NY, USA: McGraw-Hill, 1954, pp. 288–312.
[38] W. B. Rowe, H. S. Qi, M. N. Morgan, and H. W. Zheng, "The real contact length in grinding based on depth of cut and contact deflections," in *Proc. 13th Int. MATADOR Conf. UMIST*. New York, NY, USA: Macmillan, 1993, pp. 187–193.
[39] H. S. Qi, B. Mills, and W. B. Rowe, "An analysis of real contact length in abrasive machining processes using contact mechanics," *Wear*, vol. 176, no. 1, pp. 137–141, Jul. 1994, doi: 10.1016/0043-1648(94)90207-0.

MINGXIA KANG received the B.S. and M.S. degrees from the School of Mechanical Engineering, Hohai University, Jiangsu, China. She is currently pursuing the Ph.D. degree with the School of Mechanical Engineering, Southeast University. Her research interests include surface topography modeling, friction and wear characteristics analysis, and grinding process optimization.

LU ZHANG received the B.S. degree from the School of Mechanical Engineering, China University of Mining and Technology, Jiangsu, China, and the M.S. degree from the School of Mechanical Engineering, Southeast University, Jiangsu, where he is currently pursuing the master's degree. His research interests include grinding vibration and surface quality analysis.

WENCHENG TANG received the B.S., M.S., and Ph.D. degrees from the School of Mechanical Engineering, Southeast University, Jiangsu, China. He is currently a Professor and the Former Dean of the School of Mechanical Engineering, Southeast University. His research interests are focused on CAD/CAE/CAM, friction and wear of functional parts, static-dynamic analysis and optimization design of structural parts, and computer integrated manufacturing systems.